Plume Origin Localisation with Computer Vision

Jake Wilson[*]
GHGSat Inc.
London, United Kingdom

Victoria Foing[*†]
GHGSat Inc.
London, United Kingdom

Simon Andersson-Bastable
GHGSat Inc.
London, United Kingdom

Amanda Delgado-Recke
GHGSat Inc.
London, United Kingdom

Jack Hayden
GHGSat Inc.
London, United Kingdom

Dylan Jervis
GHGSat Inc.
Montreal, Canada

Krishna Mooroogen
GHGSat Inc.
London, United Kingdom

Abstract

Satellite remote sensing has become a critical tool for monitoring, measuring, and mitigating methane emissions globally. Reliable attribution of methane plumes to their source facility is needed to enable emission mitigation action, robust emissions accounting, and regulatory oversight. Although experts can manually attribute plumes to individual facilities, automated approaches are required for consistency, scalability, and transparency. Here, we provide a methodology to automatically estimate the source location of a plume as a spatial probability. Plume origin estimation is an essential component of attributing plumes to their source facility. We train a neural network to estimate a confidence region for the location of the plume source. The model achieves good accuracy, with 65.1% predicted origin points falling within 100 m (4 pixels) of an expert-annotated point, and a median distance error of 64.2m ($\sim$ 3 pixels). We demonstrate that the predicted origin probability is well-calibrated by comparing the percentage of expert origins which fall into different confidence region bins. We apply this methodology to methane plumes in GHGSat satellite imagery, but the framework could be adapted to other sensors and types of plumes.

1 Introduction

Methane emitted into the atmosphere strongly absorbs outgoing terrestrial infrared radiation and therefore contributes significantly to climate change (IPCC, 2021). Direct anthropogenic sources of methane include fossil fuel production (particularly in the oil and gas sector), agriculture, waste, biomass, and biofuel burning (Saunois et al., 2025). Due to its shorter atmospheric lifetime and higher warming potential, reducing methane emissions is seen as an effective tool to slow near-term warming (Ocko et al., 2021).

Satellite monitoring has emerged as a promising technology for identifying sources of methane emissions (Jacob et al., 2022). GHGSat operates a constellation of 14 satellites equipped with short-wave infrared sensors (Jervis et al., 2021). These sensors are used to measure the enhancement

[*]Equal contribution.
[†]Corresponding author: vfoing@ghgsat.com

Preprint.

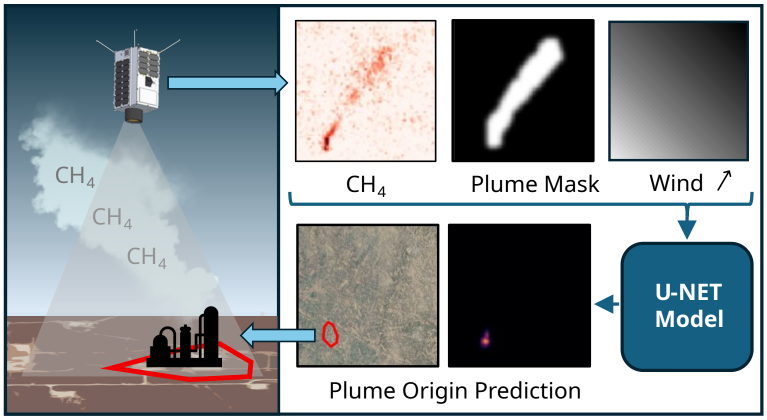

of methane above the atmospheric background with a spatial resolution of $\approx 25\,\mathrm{m}$ (Ramier et al., 2025).

Areas of strong methane enhancements may indicate a plume, an event related to the release of methane. Plumes may originate from point sources, a highly localised area of space such as an individual piece of equipment, or from more diffuse area sources, such as landfills. The form and size of a plume is determined by the emissions rate, atmospheric dispersion and local topography (Jongaramrungruang et al., 2019; Jacob et al., 2022).

Once detected, reliable attribution of methane plumes to their source is needed to enable emission mitigation action, robust emissions accounting and regulatory oversight. The first step to attribution is to identify the origin location of the plume.

Human experts estimate the location of the point-source origin of a plume by considering the speed and direction of the wind, the concentration gradient and form of the methane plume itself, high-resolution visible imagery and the location of historical emissions. Two key factors make this task particularly challenging, namely low wind speeds and turbulent atmospheric conditions that can create plumes with diffuse and complex forms.

We estimate the plume origin as a spatial probability field rather than a single point location. A spatial probability estimate can capture uncertainty in origin estimation and be used to probabilistically attribute to individual facilities. Doing this at scale with human experts is challenging, as it is time-consuming and prone to inconsistency. This motivates an automated methodology by which the origin location of methane plumes can be estimated in a consistent and repeatable way.

2 Related Work

Several approaches for estimating the source location of plumes exist, at different scales, often in the context of identifying sources of pollution. A combination of forward simulation of plumes and inverse modelling is a common approach to estimate the source location of plumes. At the meteorological microscale (<2km), Gaussian dispersion models are often used to describe the advection of pollution from source (Stockie, 2011). Such models have been used to estimate the source location of plumes from ground sensor measurements (Daniels et al., 2024; Kumar et al., 2022; Newman et al., 2024).

Computational fluid dynamics (CFD) approaches such as Large Eddy Simulations capture complex turbulence (e.g. WRF-LES)(Moeng et al., 2007) and have been used to simulate methane plumes (Fish et al., 2025). However, such simulations are computationally expensive and difficult to parameterize; especially when sampling parameter space for inversion. The computational cost of CFD simulations can be reduced by using machine-learned surrogate models and have been used to give a posterior estimate of the source location from controlled-release methane plumes (Newman et al., 2025).

At the mesoscale (2 km to 200 km), back trajectories can be used to estimate the source region of a plume. Models such as the HYSPLIT model from NOAA use gridded meteorological data as input (Stein et al., 2015). Back trajectories from HYSPLIT have been used to interpret methane detected from aircraft-based sensors (Kelly et al., 2022; Peischl et al., 2015; Ren et al., 2018). While plumes can span large areas, for example Watine-Guiu et al. (2023) observed a plume spanning over 80 km in length, most of the plumes seen by GHGSat satellites span several kilometers, i.e. at the border between microscale (<2km) and mesoscale (2 km to 200 km).

Deep learning approaches using neural networks have been reported for automatically detecting methane plumes (Joyce et al., 2023; Radman et al., 2023; Rouet-Leduc and Hulbert, 2024; Schuit et al., 2023) and estimating their emissions rate (Bruno et al., 2024; Ouerghi et al., 2025) using satellite imagery. A series of machine learning approaches were used to quantify the emissions rate and estimate the source location of plumes detected in Sentinel 5P satellite imagery (Yazdinejad et al., 2025).

Algorithm approaches that combine information from multiple plumes have been used to estimate a source location, for example, a wind-rotation method was used to estimate the source location of methane plumes detected in Sentinel 5P imagery (Maasakkers et al., 2022). Using wind direction, plumes were rotated so that they aligned North, helping to narrow down a potential source location. While this approach is effective for sources that emit regularly or are persistent, it cannot be applied in cases where only a single plume has been observed.

2.1 Our Contribution

We present a deep learning approach to estimate the source region of methane plumes from GHGSat imagery. The model predicts a spatial probability map of the plume origin using three input channels: the methane signal to error ratio, a binary mask delineating the extent of a plume, and a graphical representation of wind direction and speed. The model is trained and validated on 10,000 expert-annotated plumes from oil and gas sites across the globe. We outline an approach to validate the calibration of the resulting spatial probability maps.

3 Method

A computer vision model is trained to predict the origin location of a plume. The model requires three input channels: 1) the spatial distribution of methane signal to error ratio (SER), 2) a plume mask, and 3) a graphical representation of wind speed and direction (Figure 1). The model outputs a single channel on the same spatial frame of reference as inputs 1) and 2).

3.1 Design and Selection of Input Channels

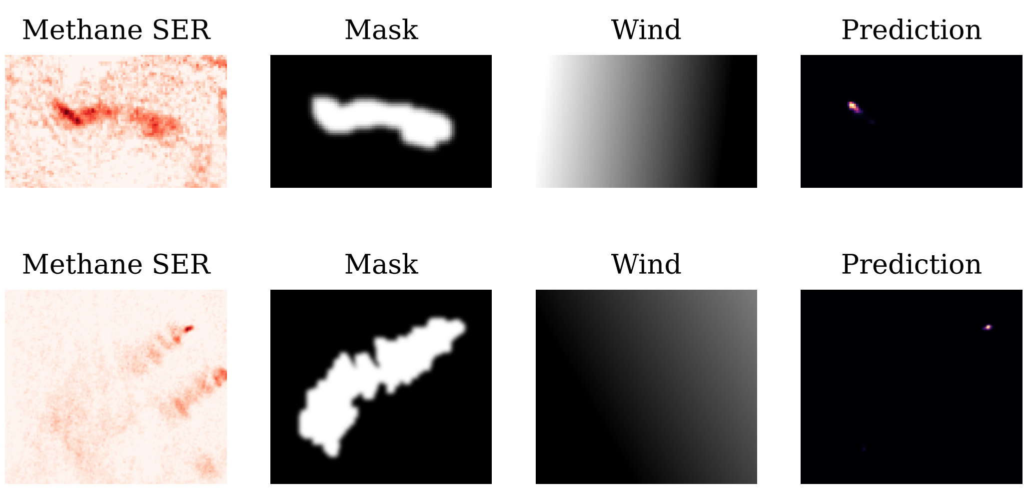

Figure 1: Plume origin model inputs and output.

The spatial distribution of methane is a crucial feature for localising the emission origin. Typically, plumes exhibit higher methane column density near the origin, and lower methane column density downwind due to advection. For GHGSat imagery, the methane signal to error ratio is obtained by dividing the methane concentration above background by a posterior error estimate. We use the methane SER (signal-to-error ratio) rather than the raw methane layer because it reduces artifacts (by construction) and therefore better reveals the true plume enhancement. The mask input channel is included to focus the model on key features in the methane channel, for example, on a single plume when multiple plumes are present (Figure 1). The binary mask delineates the extent of a plume and is created by expert operators during processing. Typically a mask can be produced using segmentation models or masking algorithms. A Gaussian blur is applied to the mask in order to make the model more robust to different masking algorithms. The final input channel is a graphical representation of wind direction and wind speed. Wind direction is represented by the direction of a gradient (where wind blows from light to dark), while the speed is represented by the magnitude (Figure 1). Wind direction is a key feature for locating the origin, especially when the methane channel lacks distinctive features. Wind speed helps to contextualise wind direction. At very low wind speeds, methane is not advected and the importance of wind direction is diminished. High-resolution visible imagery was not included in the model design, as the method focuses on estimating the origin of a plume from methane and wind information alone, without prior information from features on the ground.

3.2 Dataset Selection

Training, validation, and testing data is restricted to plumes originating from oil and gas point sources only. Plumes that have drifted from the source are excluded from the dataset. A ground-truth dataset is used to train the model, collected over time by expert operators at GHGSat. During annotation, operators select a single point in space that best represents the plume origin. The operators inform their decision using an image of the plume, knowledge of wind speed and wind direction, knowledge of previous emissions, location of facilities, as well as high-resolution visible satellite imagery.

3.3 Spatial Representation

The spatial domain of interest is represented as a finite grid of pixels. The choice of spatial domain and pixel size is determined by the field of view and the resolution of the sensor. The spatial extent of input and target images is determined using a buffer of 20 pixels ($\approx 500\,\text{m}$) around the plume mask and a pixel size of 25 m (the spatial resolution of GHGSat imagery). Plume masks vary in size, therefore to maintain a consistent input dimension, inputs and targets are padded with zeros to a size of 256 x 256 pixels before training. Padding is used instead of resizing to a fixed size to avoid deforming patterns in the image and interpolation artifacts (Hashemi, 2019). These dimensions correspond to a real world size of approximately 6.4 km x 6.4 km. A small proportion of inputs with plume masks and a buffer exceeding this spatial extent are excluded from the training dataset. Including them would require increasing the model's input size and computational cost, even though they only account for a small fraction of the total dataset.

3.4 Target Design and Interpretation

The probability π_{ij} that the true origin O is located within pixel $\mathrm{A_{ij}}$, for row i and column j, is defined as:

$$\pi_{ij} = P(O \in A_{ij}), \quad \pi_{ij} \geq 0, \quad \sum_{ij \in P} \pi_{ij} = 1.$$

To create the target for training, the expert-annotated origin point is mapped to a single pixel (value = 1) within the input's spatial reference frame:

$$\pi_{ij} = \begin{cases} 1, & \text{for the pixel containing } O, \\ 0, & \text{otherwise.} \end{cases}$$

Using this target formulation assumes complete certainty in the annotated origin location. However, it could be extended to encode spatial uncertainty, for example a Gaussian centred on the estimated origin. During training and inference, the model is not constrained to preserve the normalization condition $\sum_{ij} \pi_{ij} = 1$. Consequently, after inference, L1 normalization (division by the sum of all pixel values) is applied to the predicted output so that the resulting pixel-level probabilities sum to one. This postprocessing step allows the model output to be interpreted as a spatial probability distribution reflecting relative certainty across the image.

3.5 Training

The model is trained on 6667 samples and validated on 3333 samples for 20 epochs. Augmentations are applied to training samples, including random rotations of (-30,30) degrees and flips consistently on all three input channels. Methane SER and wind input channels are preprocessed using min/max scaler transforms (Table 1). An Adam optimizer with batch size of 32 and learning rate of 0.001 is used (Kingma and Ba, 2014). A binary cross entropy loss function with sigmoid activation is used. Loss masking is applied to set the loss values in padded regions to 0. A positive class weighting of 10 is used for every sample to reduce class imbalance. A U-Net with ResNet50 backbone is initialized with weights from an ImageNet trained model (He et al., 2016; Ronneberger et al., 2015). The U-Net architecture is selected for its suitability for pixel-level predictions (Ronneberger et al., 2015). The model is built with the Segmentation Models Pytorch package in Pytorch (Iakubovskii, 2019; Paszke et al., 2019) and all training is performed on a single NVIDIA A10G (22GB VRAM) GPU. The model from the final checkpoint was selected, as the validation loss had plateaued and showed no meaningful divergence from the best checkpoint.

Table 1: Min/max scaler transform parameters.

Channel	Min	Max
Methane SER	0	Max
Wind Speed [m/s]	1	6

3.6 Defining Confidence Region

A confidence region C_α is the collection of pixels with the highest probabilities whose total probability mass sums to a specified proportion α, where $0 < \alpha \leq 1$. This region provides both an interpretable summary of a complex spatial probability field and a practical means of simplifying storage, visualization, and large-scale search. In addition, confidence regions are useful for validation, as they allow comparison of predicted spatial probability distributions against known origin locations within a consistent probabilistic framework. To construct the confidence region, the pixels are first sorted in order of decreasing probability $\hat{\pi}_{(m)}$:

$$\hat{\pi}_{(1)} \geq \hat{\pi}_{(2)} \geq \cdots \geq \hat{\pi}_{(n)},$$

where $\hat{\pi}_{(m)}$ denotes the m-th largest probability value across all pixels and n the total number of pixels. The cutoff rank r_α is then defined as the smallest integer such that the cumulative probability mass reaches or exceeds the desired level α:

$$r_\alpha = \min \left\{ r : \sum_{m=1}^{r} \hat{\pi}_{(m)} \geq \alpha \right\}.$$

Finally, the confidence region C_α is defined as the set of pixels corresponding to these top r_α probabilities:

$$C_\alpha = \{A_{(1)}, A_{(2)}, \ldots, A_{(r_\alpha)}\}.$$

The larger the choice of α, the greater the spatial extent of the confidence region. Due to the use of a discrete pixel space, the smallest possible confidence region encompasses a single pixel. The largest possible confidence region spans the entire image. There is no requirement for the confidence region to be bounded by a single closed contour, instead it can consist of multiple separate regions in the image.

4 Results

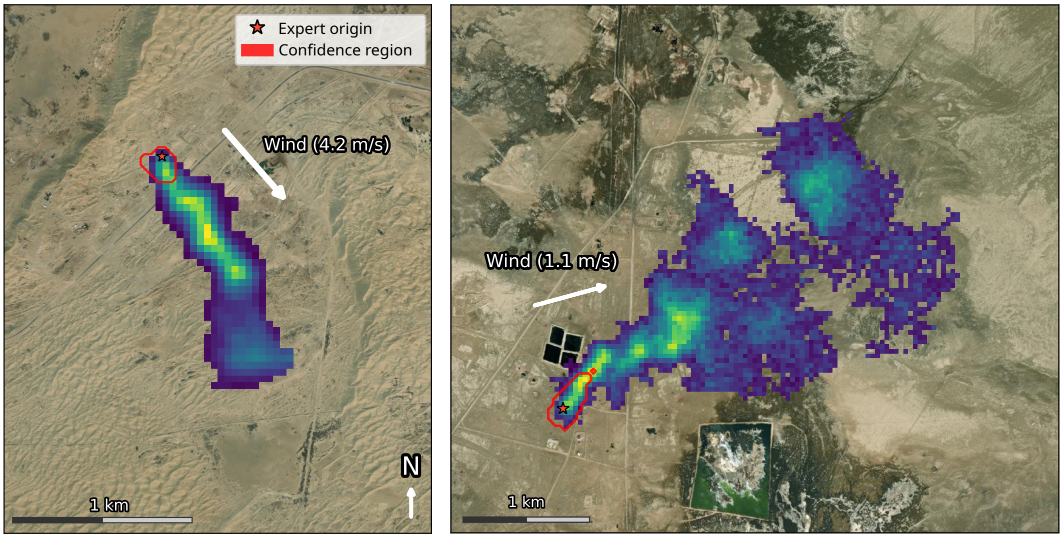

Figure 2: The origin confidence region (red contour) is shown for two plumes over satellite imagery from ESRI. The expert-annotated origin is shown as a red star symbol and the wind is blowing in the direction of the arrows. Left) the plume is advected at a higher wind speed (4.2 m/s) and the origin confidence region is small relative to the plume size. Right) the lower wind speed (1.1 m/s) results in pooling and more ambiguity in the true source location, with two separate confidence regions of different sizes. Map image is the intellectual property of Esri and is used herein under license. Copyright © 2025 Esri and its licensors. All rights reserved.

4.1 Estimating Confidence Region

For practical applications, such as visualisation and computation, it is useful to define a single confidence region. We choose the 0.8 confidence region ($\alpha = 0.8$), capturing the most probable 80% of the spatial probability mass (Figure 2). Two example plumes are shown alongside the 80% confidence regions estimated by the plume origin model. The methane signal to error ratio is overlaid on high-resolution satellite imagery (Esri, 2025). Both plumes were observed in Turkmenistan by GHGSat satellites. In the left example, a North Westerly wind with moderate speed (4.2 m/s) advects the plume. In the right example, the methane enhancement is indicative of pooling at low wind speeds (1.1 m/s). The estimated confidence region (red contour) is small compared to the plume size. The expert annotation is shown by the red star. In both examples, the expert annotation is inside of the 80% confidence region ($\alpha = 0.8$).

4.2 Validation with Point Estimation

In order to assess accuracy through a distance-based error metric with respect to the expert-annotated origin, we extract an origin point from the spatial probability distribution. We define the predicted origin as the expectation of the probability distribution. The probability expectation (centre of mass) (μ_x, μ_y) is computed as:

$$\mu_x = \sum_{x,y} x\hat{\pi}_{x,y}, \quad \mu_y = \sum_{x,y} y\hat{\pi}_{x,y} \tag{1}$$

The Euclidean distance between this expectation point and the expert annotation is computed in meters. As this work introduces both a novel method and a new proprietary dataset, direct quantitative comparison with prior approaches is not possible. Model performance is therefore evaluated against an internal non-machine learning baseline, where the centre of the pixel with the highest methane signal to error ratio intensity is selected as the origin location.

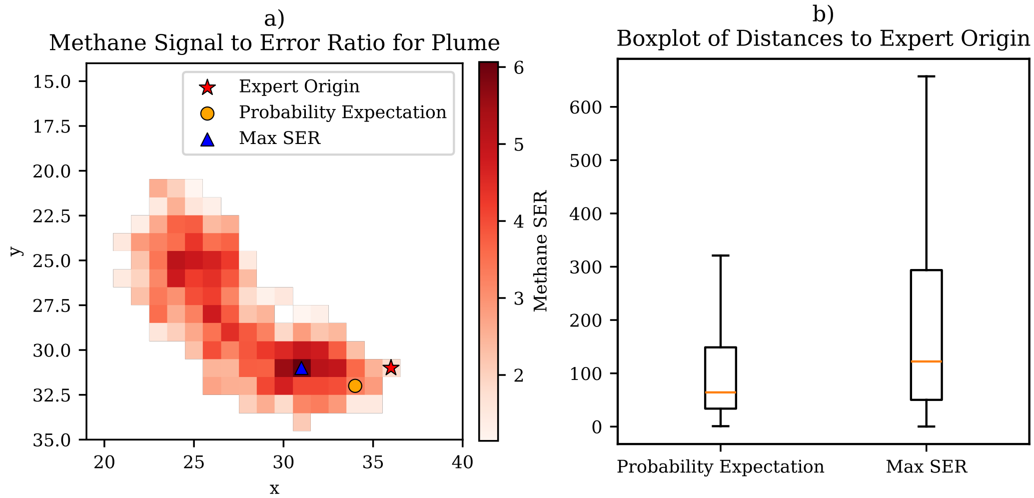

Figure 3: a) Example of Methane SER for a plume with three origin points: expert origin, predicted origin (pixel with the probability expectation from the plume origin model), and baseline (max SER) origin; b) Boxplot showing inter-quartile range (IQR) of distance (m) between the expert origin and the predicted origin and the baseline origin for held out test samples (N=3333). The box shows the IQR, whiskers extend to furthest data point lying within 1.5 $\times$ the IQR from the box. Extreme outliers are not shown.

An example methane plume is shown in 3a. The predicted origin (orange circle) is closer to the expert origin (red star) than the baseline origin (blue triangle).

Figure 3b show box plots for the distance (in meters) between the predicted origin and expert-annotated origin. For reference, a box plot of distance between the baseline origin and expert-annotated origin is also shown. The box shows the interquartile range (IQR) and whiskers extend to farthest data point lying within 1.5 $\times$ the IQR from the box. Extreme outliers are not shown. The median distance of the plume origin model was considerably lower (64.2 m) than the baseline (122.2 m). Likewise, 40.7% and 65.1% of predicted origins were within 50 m and 100 m of the expert origin, respectively, compared with only 24.9% and 44.2% for the baseline.

Table 2: Summary statistics comparing the distance between the predicted origin and expert origin with the distance between the baseline origin and expert origin.

Method	Median Distance [m]	< 50 m	< 100 m
Baseline Origin	122.2	831 (24.9%)	1474 (44.2%)
Predicted Origin	64.2	1356 (40.7%)	2169 (65.1%)

4.3 Validation with Confidence Region

The second validation approach takes into account the full probability distribution function, rather than a single point. To compare model predictions with the expert-annotated origin O it is convenient to define the metric α_O, the smallest confidence region to contain O. Let r_O be the rank of the pixel containing O, and $m = 1$ be the highest ranking pixel (largest probability value across all pixels), then:

$$\alpha_O = \sum_{m=1}^{r_O} \hat{\pi}_{(m)}.$$

A lower α_O indicates the expert-annotated origin lies within a region of high predicted probability, reflecting a confident and well-localised model prediction (see Figure 5). Higher α_O implies that the origin is only captured within a larger confidence region, indicating lower model confidence or spatial accuracy in the vicinity of the true location (see Figure 6).

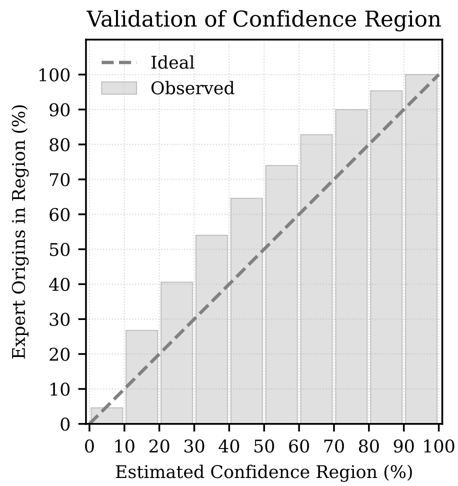

Figure 4: Validation of confidence region by comparing the estimated confidence region with the percentage of expert origins which fall within that region.

The calibration performance of the model is assessed by computing the cumulative proportion of samples with α_O less than or equal to a series of confidence thresholds. Figure 4 shows the cumulative proportions expressed as percentages across ten equal-width confidence bins (N=3333). A perfectly calibrated model would follow the 1:1 line (grey), meaning that, for example, 80% of expert origins are expected to fall within the 80% bin and only 20% of expert origins would fall in the 20% bin. In contrast, the empirical results lie consistently above this ideal line. For instance, 26.8% of expert origins fall within the 20% bin and 89.9% fall within the 80% bin. This indicates that although the model is broadly well-calibrated, probability estimates are, if anything, slightly conservative, leading to larger confidence regions and less localised predictions. Potential approaches for refining and recalibrating the model are discussed below.

5 Discussion

Our results establish that a U-Net model trained on methane signal-to-error ratio, plume shape, and wind information can localise plume origins with accuracy comparable to expert annotation, with 65.1% of predictions falling within 100m (four pixels) of the expert annotations. The model outperforms a non-machine learning baseline for which only 44.2% of predictions fall within 100m of expert annotation (Figure 3). The model performed best for samples with clear plume structures that were well aligned with wind direction, strong wind speeds and with high intensity signal to error ratios over the origin (Figure 5). Other challenging examples include samples where the plume in the observation is diffuse (see Figure 6) and the wind speed is low, or the source is intermittent. Generally, higher wind speeds, especially above 5 m/s, produced plumes with simpler structures and therefore more agreement between model predictions and expert annotations (Figure 7). In contrast, there was no clear relationship between wind direction and model performance (Figure 8).

A small number (5.9%) of samples showed a very large error (> 500 m) between the expert and predicted origin point, also illustrated by the long tailed distribution in the box plot (Figure 3). Inspection revealed that the worst performing samples were often associated with certain measurement errors. In some cases, an observation of a plume may include artifacts, a plume may be detected in the vicinity of other plumes, or a plume may be cut off at the edge of an observation. Wind direction and speed are obtained from atmospheric reanalysis models, which are gridded with relatively coarse spatial and temporal resolutions (e.g. ERA5, 9 km × 9 km, hourly) (Hersbach et al., 2020). The accuracy of these models varies spatially, meaning wind estimates carry greater uncertainty in regions where local measurements are unavailable for validation. The probability density function for some plumes exhibited multiple local maxima, such as elongated plumes with no clear directionality (for example, see Figure 6). In such cases, using the spatial expectation value to predict a single origin point may not be suitable as it can yield a point located between local maxima. Where a single origin point is required, this could be resolved by instead selecting the centre of the pixel with the highest probability value as the origin estimate (Figure 9).

Even expert annotated points carry some degree of error or uncertainty, a fact which is not represented in our training on a single target pixel. While the model is not constrained to make a single pixel prediction, exploring other representations of uncertainty during training could be advantageous. For example, aleatoric uncertainty could be represented during training by having multiple experts annotate the same plume, ambiguity in the true location would lead to a spread of target points. Alternatively, experts could annotate plumes with a plausible area, helping to capture some of the ambiguity.

The confidence region validation (Figure 4) demonstrates that the model produces well-characterized spatial probability estimates, capturing not only the most likely origin location but also the spatial extent of uncertainty around it. It suggests a higher proportion of expert origins are found in smaller confidence regions than expected, i.e. the origin model may be overly conservative in uncertainty estimates. The positive class weighting is a key hyperparameter for controlling calibration performance. With a single pixel target and a fixed input size of 256×256 pixels, the fraction of positive pixels is very low (0.0015%). As mentioned in the methods, a positive class weighting is used to reduce imbalance. Keeping the model in native resolution is also important to maintain control of this class balance. For example, resizing small images will stretch the target pixel and introduce interpolation artifacts. Given that loss masking is applied to ignore padded regions, smaller samples that do not fill the full 256×256 extent will have a higher target to background pixel ratio. Using separate positive class weightings for each sample could help to mitigate this effect and requires more exploration. While rare in this particular dataset, large plumes that exceed the input size would require a further exploration and would require an alternative tiling or resizing strategy.

In this paper, we focused on plumes observed by GHGSat satellites; however, the approach is suitable for other satellites with a similar spatial resolution such as Sentinel-2 (European Space Agency), Tanager-1 (Carbon Mapper), Landsat, EMIT, PRISMA, EnMAP, WorldView-3 (Duren et al., 2025). Beyond methane, this approach could be adapted to other use cases, such as determining the origin of smoke plumes in visible imagery. This study benefits from an abundance of annotated data for training, validation, and testing. Such data is unlikely to be available for all sensors. In the absence of real training data, an equivalent model could be trained on simulated plumes from a known origin point. Synthetic data could be generated using Gaussian dispersion models or CFD simulations such WRF-LES, as has been done previously for plume quantification and detection models (Varon et al., 2018; Jongaramrungruang et al., 2021). Finally, this study addressed point emitters, but the framework could be adapted for area emitters, such as landfills and open-pit coal mines.

One major application of representing the origin location as a spatial probability estimate is to enable the probabilistic attribution of methane plumes to source facilities or equipment. Methane plumes can span multiple source locations, whether facilities or individual pieces of equipment. In dense areas such as the Permian basin, there are many facilities in close proximity. Likewise, a single facility can contain many pieces of equipment in a small area. A single point estimate, whether from expert annotators or from automatic methods, cannot represent the uncertainty needed for this attribution. The quantitative use of spatial probability density functions to attribute methane plumes to individuals or pieces of equipment will be explored in future work.

6 Conclusions

We introduce a novel machine learning approach that gives spatial probability estimates of plume origin locations. The model uses satellite imagery of the methane signal to error ratio, a mask of the plume, and a graphical representation of wind direction and speed. We train and validate on 10,000 real-world plumes from oil and gas infrastructure around the globe and test on a further 3,333. The model achieves good accuracy, with 65.1% of predicted origins falling within 100 m (four pixels) of an expert-annotated point. Furthermore, we develop a validation framework using confidence regions to demonstrate that model predictions are well-calibrated with respect to expert-annotated points. Future work will address several key areas: (1) improving model calibration to further reduce uncertainty for emission source localisation, (2) expanding the approach to different sensors to enable emissions monitoring at various spatial and temporal scales, and (3) expanding the approach to different emission source types such as area sources to improve generalizability for other sectors.

Acknowledgements

This work was supported by the European Space Agency (ESA) through the InCubed programme.

References

Jack H. Bruno, Dylan Jervis, Daniel J. Varon, and Daniel J. Jacob. U-plume: automated algorithm for plume detection and source quantification by satellite point-source imagers. *Atmospheric Measurement Techniques*, 17:2625–2636, 5 2024. ISSN 18678548. doi: 10.5194/AMT-17-2625-2024.

William S. Daniels, Meng Jia, and Dorit M. Hammerling. Detection, localization, and quantification of single-source methane emissions on oil and gas production sites using point-in-space continuous monitoring systems. *Elementa*, 12:12016–12026, 3 2024. ISSN 23251026. doi: 10.1525/ELEMENTA.2023.00110/200346. URL `/elementa/article/12/1/00110/200346/Detection-localization-and-quantification-ofhttps://dx.doi.org/10.1525/elementa.2023.00110`.

Riley Duren, Daniel Cusworth, Alana Ayasse, Kate Howell, Alex Diamond, Tia Scarpelli, Jinsol Kim, Kelly O'neill, Judy Lai-Norling, Andrew Thorpe, Sander R. Zandbergen, Lucas Shaw, Mark Keremedjiev, Jeff Guido, Paul Giuliano, Malkam Goldstein, Ravi Nallapu, Geert Barentsen, David R. Thompson, Keely Roth, Daniel Jensen, Michael Eastwood, Frances Reuland, Taylor Adams, Adam Brandt, Eric A. Kort, James Mason, and Robert O. Green. The carbon mapper emissions monitoring system. 6 2025. doi: 10.5194/EGUSPHERE-2025-2275. URL `https://egusphere.copernicus.org/preprints/2025/egusphere-2025-2275/`.

Esri. Esri basemap. `https://www.arcgis.com/home/item.html?id=10df2279f9684e4a9f6a7f08febac2a9`, 2025.

Ryker Fish, Federico Municchi, Brennan Sprinkle, and Dorit Hammerling. A comparison of turbulent cfd with gaussian dispersion models on a methane emission test site. *Atmospheric Environment: X*, 27:100326, 8 2025. ISSN 2590-1621. doi: 10.1016/J.AEAOA.2025.100326.

Mahdi Hashemi. Enlarging smaller images before inputting into convolutional neural network: zero-padding vs. interpolation. *Journal of Big Data*, 6(1):98, 2019. ISSN 2196-1115. doi: 10.1186/s40537-019-0263-7. URL `https://journalofbigdata.springeropen.com/articles/10.1186/s40537-019-0263-7`.

Kaiming He, Xiangyu Zhang, Shaoqing Ren, and Jian Sun. Deep residual learning for image recognition, 2016. URL `http://image-net.org/challenges/LSVRC/2015/`.

Hans Hersbach, Bill Bell, Paul Berrisford, Shoji Hirahara, András Horányi, Joaquín Muñoz-Sabater, Julien Nicolas, Carole Peubey, Raluca Radu, Dinand Schepers, Adrian Simmons, Cornel Soci, Saleh Abdalla, Xavier Abellan, Gianpaolo Balsamo, Peter Bechtold, Gionata Biavati, Jean Bidlot, Massimo Bonavita, Giovanna De Chiara, Per Dahlgren, Dick Dee, Michail Diamantakis, Rossana Dragani, Johannes Flemming, Richard Forbes, Manuel Fuentes, Alan Geer, Leo Haimberger, Sean Healy, Robin J. Hogan, Elías Hólm, Marta Janisková, Sarah Keeley, Patrick Laloyaux, Philippe Lopez, Cristina Lupu, Gabor Radnoti, Patricia de Rosnay, Iryna Rozum, Freja Vamborg, Sebastien Villaume, and Jean Noël Thépaut. The era5 global reanalysis. *Quarterly Journal of the Royal Meteorological Society*, 146:1999–2049, 7 2020. ISSN 1477-870X. doi: 10.1002/QJ.3803. URL `https://onlinelibrary.wiley.com/doi/full/10.1002/qj.3803https://onlinelibrary.wiley.com/doi/abs/10.1002/qj.3803https://rmets.onlinelibrary.wiley.com/doi/10.1002/qj.3803`.

Pavel Iakubovskii. Segmentation models pytorch, 2019. URL `https://github.com/qubvel-org/segmentation_models.pytorch?tab=readme-ov-file#citing`.

IPCC. Chapter 7: The earth's energy budget, climate feedbacks, and climate sensitivity. *In* Climate Change 2021: The Physical Science Basis. Contribution of Working Group I to the Sixth Assessment Report of the Intergovernmental Panel on Climate Change, 2021. URL `https://www.ipcc.ch/report/ar6/wg1/chapter/chapter-7/`. Accessed: 2025-10-30.

Daniel J. Jacob, Daniel J. Varon, Daniel H. Cusworth, Philip E. Dennison, Christian Frankenberg, Ritesh Gautam, Luis Guanter, John Kelley, Jason McKeever, Lesley E. Ott, Benjamin Poulter, Zhen Qu, Andrew K. Thorpe, John R. Worden, and Riley M. Duren. Quantifying methane emissions from the global scale down to point sources using satellite observations of atmospheric methane. *Atmospheric Chemistry and Physics*, 22:9617–9646, 7 2022. ISSN 16807324. doi: 10.5194/ACP-22-9617-2022.

Dylan Jervis, Jason McKeever, Berke O.A. Durak, James J. Sloan, David Gains, Daniel J. Varon, Antoine Ramier, Mathias Strupler, and Ewan Tarrant. The ghgsat-d imaging spectrometer. *Atmospheric Measurement Techniques*, 14:2127–2140, 3 2021. ISSN 18678548. doi: 10.5194/AMT-14-2127-2021.

S. Jongaramrungruang, C. Frankenberg, G. Matheou, A. K. Thorpe, D. R. Thompson, L. Kuai, and R. M. Duren. Towards accurate methane point-source quantification from high-resolution 2-d plume imagery. *Atmospheric Measurement Techniques*, 12(12):6667–6681, 2019. doi: 10.5194/amt-12-6667-2019. URL https://amt.copernicus.org/articles/12/6667/2019/.

S. Jongaramrungruang, G. Matheou, A. K. Thorpe, Z.-C. Zeng, and C. Frankenberg. Remote sensing of methane plumes: instrument tradeoff analysis for detecting and quantifying local sources at global scale. *Atmospheric Measurement Techniques*, 14(12):7999–8017, 2021. doi: 10.5194/amt-14-7999-2021. URL https://amt.copernicus.org/articles/14/7999/2021/.

Peter Joyce, Cristina Ruiz Villena, Yahui Huang, Alex Webb, Manuel Gloor, Fabien H. Wagner, Martyn P. Chipperfield, Rocío Barrio Guilló, Chris Wilson, and Hartmut Boesch. Using a deep neural network to detect methane point sources and quantify emissions from prisma hyperspectral satellite images. *Atmospheric Measurement Techniques*, 16:2627–2640, 5 2023. ISSN 18678548. doi: 10.5194/AMT-16-2627-2023.

Bryce F.J. Kelly, Xinyi Lu, Stephen J. Harris, Bruno G. Neininger, Jorg M. Hacker, Stefan Schwietzke, Rebecca E. Fisher, James L. France, Euan G. Nisbet, David Lowry, Carina Van Der Veen, Malika Menoud, and Thomas Röckmann. Atmospheric methane isotopes identify inventory knowledge gaps in the surat basin, australia, coal seam gas and agricultural regions. *Atmospheric Chemistry and Physics*, 22:15527–15558, 12 2022. ISSN 16807324. doi: 10.5194/ACP-22-15527-2022.

Diederik P. Kingma and Jimmy Lei Ba. Adam: A method for stochastic optimization. *3rd International Conference on Learning Representations, ICLR 2015 - Conference Track Proceedings*, 12 2014. URL https://arxiv.org/abs/1412.6980v9.

Pramod Kumar, Grégoire Broquet, Christopher Caldow, Olivier Laurent, Susan Gichuki, Ford Cropley, Camille Yver-Kwok, Bonaventure Fontanier, Thomas Lauvaux, Michel Ramonet, Adil Shah, Guillaume Berthe, Frédéric Martin, Olivier Duclaux, Catherine Juery, Caroline Bouchet, Joseph Pitt, and Philippe Ciais. Near-field atmospheric inversions for the localization and quantification of controlled methane releases using stationary and mobile measurements. *Quarterly Journal of the Royal Meteorological Society*, 148:1886–1912, 4 2022. ISSN 1477-870X. doi: 10.1002/QJ.4283. URL https://onlinelibrary.wiley.com/doi/full/10.1002/qj.4283https://onlinelibrary.wiley.com/doi/abs/10.1002/qj.4283https://rmets.onlinelibrary.wiley.com/doi/10.1002/qj.4283.

Joannes D. Maasakkers, Daniel J. Varon, Aldís Elfarsdóttir, Jason McKeever, Dylan Jervis, Gourav Mahapatra, Sudhanshu Pandey, Alba Lorente, Tobias Borsdorff, Lodewijck R. Foorthuis, Berend J. Schuit, Paul Tol, Tim A. van Kempen, Richard van Hees, and Ilse Aben. Using satellites to uncover large methane emissions from landfills. *Science Advances*, 8(32):eabn9683, 2022. doi: 10.1126/sciadv.abn9683. URL https://www.ncbi.nlm.nih.gov/pmc/articles/PMC9365275/.

Chin Hoh Moeng, Jimy Dudhia, Joe Klemp, and Peter Sullivan. Examining two-way grid nesting for large eddy simulation of the pbl using the wrf model. *Monthly Weather Review*, 135:2295–2311, 6 2007. ISSN 1520-0493. doi: 10.1175/MWR3406.1. URL https://journals.ametsoc.org/view/journals/mwre/135/6/mwr3406.1.xml.

Thomas Newman, Christopher Nemeth, Matthew Jones, and Philip Jonathan. Probabilistic inversion modeling of gas emissions: A gradient-based mcmc estimation of gaussian plume parameters. *arXiv*, page arXiv:2408.01298, 10 2024. doi: 10.48550/ARXIV.2408.01298. URL https://ui.adsabs.harvard.edu/abs/2024arXiv240801298N/abstract.

Thomas Newman, Christopher Nemeth, Matthew Jones, and Philip Jonathan. Deep learning surrogates for real-time gas emission inversion. 6 2025. URL http://arxiv.org/abs/2506.14597.

Ilissa B. Ocko, Tianyi Sun, Drew Shindell, Michael Oppenheimer, Alexander N. Hristov, Stephen W. Pacala, Denise L. Mauzerall, Yangyang Xu, and Steven P. Hamburg. Acting rapidly to deploy readily available methane mitigation measures by sector can immediately slow global warming. *Environmental Research Letters*, 16:054042, 5 2021. ISSN 1748-9326. doi: 10.1088/1748-9326/ABF9C8. URL https://iopscience.iop.org/article/10.1088/1748-9326/abf9c8https://iopscience.iop.org/article/10.1088/1748-9326/abf9c8/meta.

Elyes Ouerghi, Thibaud Ehret, Gabriele Facciolo, Enric Meinhardt, Rodolphe Marion, and Jean-Michel Morel. Tightening-up methane plume source rate estimation in enmap and prisma images. 4 2025. doi: 10.5194/EGUSPHERE-2025-1075. URL https://egusphere.copernicus.org/preprints/2025/egusphere-2025-1075/.

Adam Paszke, Sam Gross, Francisco Massa, Adam Lerer, James Bradbury Google, Gregory Chanan, Trevor Killeen, Zeming Lin, Natalia Gimelshein, Luca Antiga, Alban Desmaison, Andreas Köpf Xamla, Edward Yang, Zach Devito, Martin Raison Nabla, Alykhan Tejani, Sasank Chilamkurthy, Qure Ai, Benoit Steiner, Lu Fang Facebook, Junjie Bai Facebook, and Soumith Chintala. Pytorch: An imperative style, high-performance deep learning library. *Advances in Neural Information Processing Systems*, 32, 2019.

J. Peischl, T. B. Ryerson, K. C. Aikin, J. A. De Gouw, J. B. Gilman, J. S. Holloway, B. M. Lerner, R. Nadkarni, J. A. Neuman, J. B. Nowak, M. Trainer, C. Warneke, and D. D. Parrish. Quantifying atmospheric methane emissions from the haynesville, fayetteville, and northeastern marcellus shale gas production regions. *Journal of Geophysical Research: Atmospheres*, 120:2119–2139, 3 2015. ISSN 2169-8996. doi: 10.1002/2014JD022697. URL https://onlinelibrary.wiley.com/doi/full/10.1002/2014JD022697https://onlinelibrary.wiley.com/doi/abs/10.1002/2014JD022697https://agupubs.onlinelibrary.wiley.com/doi/10.1002/2014JD022697.

Ali Radman, Masoud Mahdianpari, Daniel J. Varon, and Fariba Mohammadimanesh. S2metnet: A novel dataset and deep learning benchmark for methane point source quantification using sentinel-2 satellite imagery. *Remote Sensing of Environment*, 295:113708, 9 2023. ISSN 0034-4257. doi: 10.1016/J.RSE.2023.113708.

Antoine Ramier, Marianne Girard, Dylan Jervis, Jean Philippe MacLean, David Marshall, Jason McKeever, Mathias Strupler, Ewan Tarrant, and David Young. High-resolution methane detection with the ghgsat constellation. *Copyright: International Astronautical Federation*, page 2023, 5 2025. doi: 10.31223/X5FF0X. URL https://eartharxiv.org/repository/view/9307/.

Xinrong Ren, Olivia E. Salmon, Jonathan R. Hansford, Doyeon Ahn, Dolly Hall, Sarah E. Benish, Phillip R. Stratton, Hao He, Sayantan Sahu, Courtney Grimes, Alexie M.F. Heimburger, Cory R. Martin, Mark D. Cohen, Barbara Stunder, Ross J. Salawitch, Sheryl H. Ehrman, Paul B. Shepson, and Russell R. Dickerson. Methane emissions from the baltimore-washington area based on airborne observations: Comparison to emissions inventories. *Journal of Geophysical Research: Atmospheres*, 123:8869–8882, 8 2018. ISSN 2169-8996. doi: 10.1029/2018JD028851. URL https://onlinelibrary.wiley.com/doi/full/10.1029/2018JD028851https://onlinelibrary.wiley.com/doi/abs/10.1029/2018JD028851https://agupubs.onlinelibrary.wiley.com/doi/10.1029/2018JD028851.

Olaf Ronneberger, Philipp Fischer, and Thomas Brox. U-net: Convolutional networks for biomedical image segmentation. *Lecture Notes in Computer Science (including subseries Lecture Notes in Artificial Intelligence and Lecture Notes in Bioinformatics)*, 9351:234–241, 2015. ISSN 1611-3349. doi: 10.1007/978-3-319-24574-4_28. URL https://link.springer.com/chapter/10.1007/978-3-319-24574-4_28.

Bertrand Rouet-Leduc and Claudia Hulbert. Automatic detection of methane emissions in multispectral satellite imagery using a vision transformer. *Nature Communications 2024 15:1*, 15:1–9, 5 2024. ISSN 2041-1723. doi: 10.1038/s41467-024-47754-y. URL https://www.nature.com/articles/s41467-024-47754-y.

Marielle Saunois, Adrien Martinez, Benjamin Poulter, Zhen Zhang, Peter A. Raymond, Pierre Regnier, Josep G. Canadell, Robert B. Jackson, Prabir K. Patra, Philippe Bousquet, Philippe Ciais, Edward J. Dlugokencky, Xin Lan, George H. Allen, David Bastviken, David J. Beerling, Dmitry A. Belikov, Donald R. Blake, Simona Castaldi, Monica Crippa, Bridget R. Deemer, Fraser Dennison, Giuseppe Etiope, Nicola Gedney, Lena Höglund-Isaksson, Meredith A. Holgerson, Peter O. Hopcroft, Gustaf Hugelius, Akihiko Ito, Atul K. Jain, Rajesh Janardanan, Matthew S. Johnson, Thomas Kleinen, Paul B. Krummel, Ronny Lauerwald, Tingting Li, Xiangyu Liu, Kyle C. Mcdonald, Joe R. Melton, Jens Mühle, Jurek Müller, Fabiola Murguia-Flores, Yosuke Niwa, Sergio Noce, Shufen Pan, Robert J. Parker, Changhui Peng, Michel Ramonet, William J. Riley, Gerard Rocher-Ros, Judith A. Rosentreter, Motoki Sasakawa, Arjo Segers, Steven J. Smith, Emily H. Stanley, Joël Thanwerdas, Hanqin Tian, Aki Tsuruta, Francesco N. Tubiello, Thomas S. Weber, Guido R. Van Der Werf, Douglas E.J. Worthy, Yi Xi, Yukio Yoshida, Wenxin Zhang, Bo Zheng, Qing Zhu, Qiuan Zhu, and Qianlai Zhuang. Global methane budget 2000-2020. *Earth System Science Data*, 17:1873–1958, 5 2025. ISSN 18663516. doi: 10.5194/ESSD-17-1873-2025.

B. J. Schuit, J. D. Maasakkers, P. Bijl, G. Mahapatra, A.-W. van den Berg, S. Pandey, A. Lorente, T. Borsdorff, S. Houweling, D. J. Varon, J. McKeever, D. Jervis, M. Girard, I. Irakulis-Loitxate, J. Gorroño, L. Guanter, D. H. Cusworth, and I. Aben. Automated detection and monitoring of methane super-emitters using satellite data. *Atmospheric Chemistry and Physics*, 23(16): 9071–9098, 2023. doi: 10.5194/acp-23-9071-2023. URL `https://acp.copernicus.org/articles/23/9071/2023/`.

A. F. Stein, R. R. Draxler, G. D. Rolph, B. J.B. Stunder, M. D. Cohen, and F. Ngan. Noaa's hysplit atmospheric transport and dispersion modeling system. *Bulletin of the American Meteorological Society*, 96:2059–2077, 12 2015. ISSN 0003-0007. doi: 10.1175/BAMS-D-14-00110.1. URL `https://journals.ametsoc.org/view/journals/bams/96/12/bams-d-14-00110.1.xml`.

John M. Stockie. The mathematics of atmospheric dispersion modeling. *https://doi.org/10.1137/10080991X*, 53:349–372, 5 2011. ISSN 00361445. doi: 10.1137/10080991X. URL `https://epubs.siam.org/doi/10.1137/10080991X`.

D. J. Varon, D. J. Jacob, J. McKeever, D. Jervis, B. O. A. Durak, Y. Xia, and Y. Huang. Quantifying methane point sources from fine-scale satellite observations of atmospheric methane plumes. *Atmospheric Measurement Techniques*, 11(10):5673–5686, 2018. doi: 10.5194/amt-11-5673-2018. URL `https://amt.copernicus.org/articles/11/5673/2018/`.

Marc Watine-Guiu, Daniel J. Varon, Itziar Irakulis-Loitxate, Nicholas Balasus, and Daniel J. Jacob. Geostationary satellite observations of extreme and transient methane emissions from oil and gas infrastructure. *Proceedings of the National Academy of Sciences of the United States of America*, 120:e2310797120, 12 2023. ISSN 10916490. doi: 10.1073/PNAS.2310797120/SUPPL_FILE/PNAS.2310797120.SAPP.PDF. URL `https://www.pnas.org/doi/abs/10.1073/pnas.2310797120`.

Abbas Yazdinejad, Hao Wang, and Jude Kong. Advanced ai-driven methane emission detection, quantification, and localization in canada: A hybrid multi-source fusion framework. *Science of The Total Environment*, 998:180142, 10 2025. ISSN 0048-9697. doi: 10.1016/J.SCITOTENV.2025.180142. URL `https://linkinghub.elsevier.com/retrieve/pii/S0048969725017826`.

A Appendix

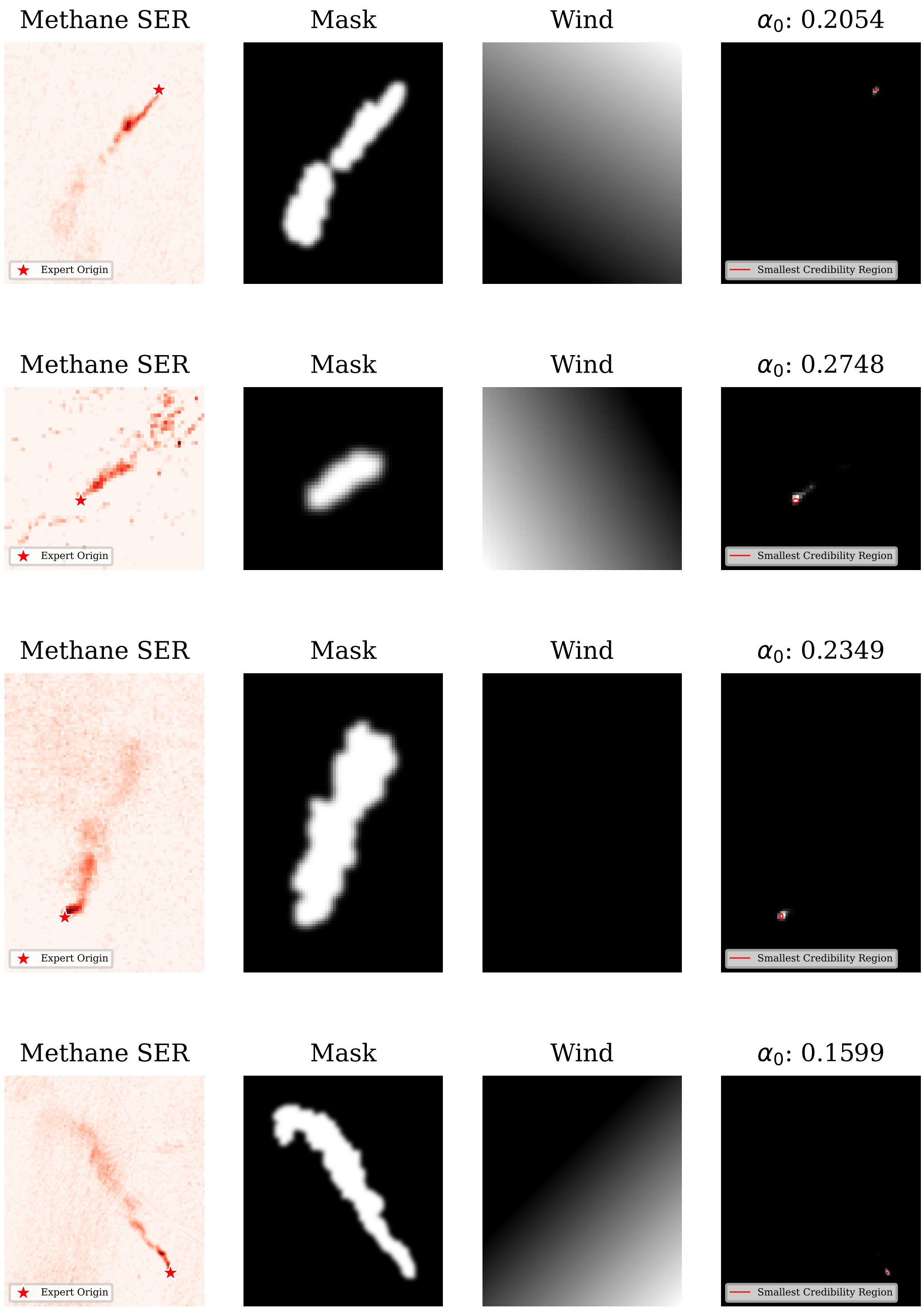

Figure 5: Examples of plume origin predictions that are localised near the expert origin point. For each example, the smallest confidence region that contains the expert origin is comprised of few pixels.

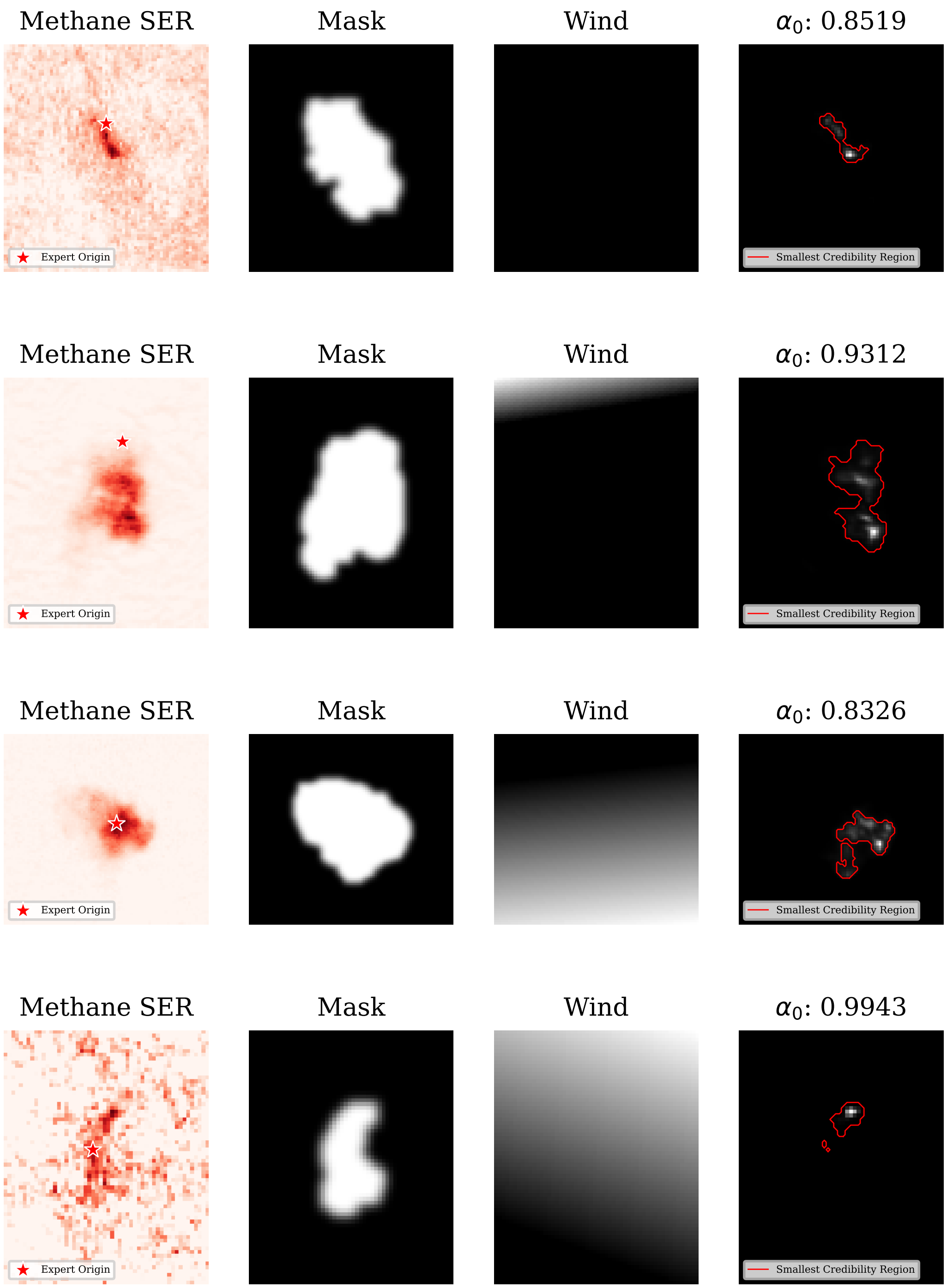

Figure 6: Examples of plume origin predictions that are not localised near the expert origin point. For each example, the smallest confidence region that contains the expert origin is comprised of several pixels. In some examples, the confidence region consists of multiple regions.

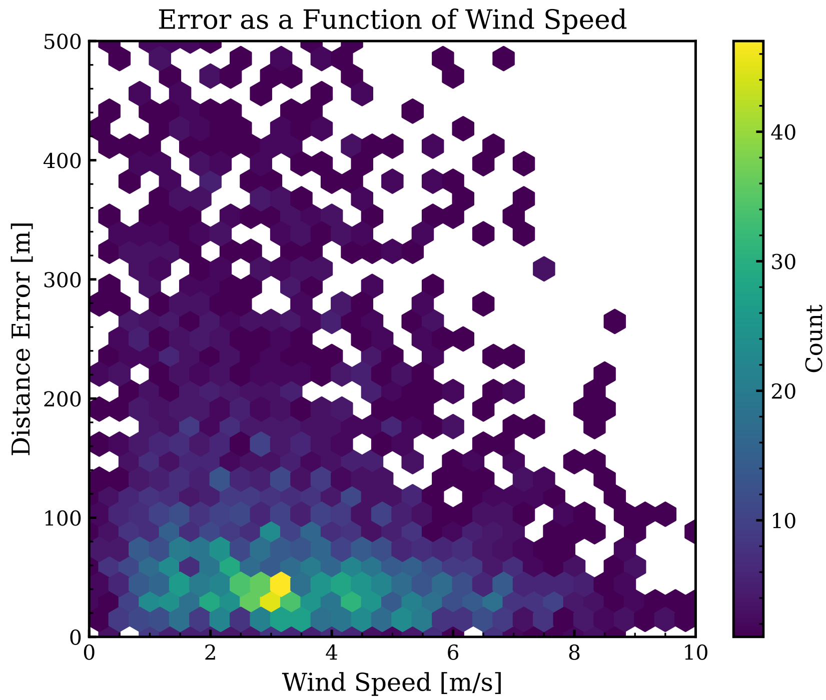

Figure 7: Distance error (m) as a function of wind speed (m/s) on the test set, showing smaller distance errors for higher wind speeds above 5 m/s.

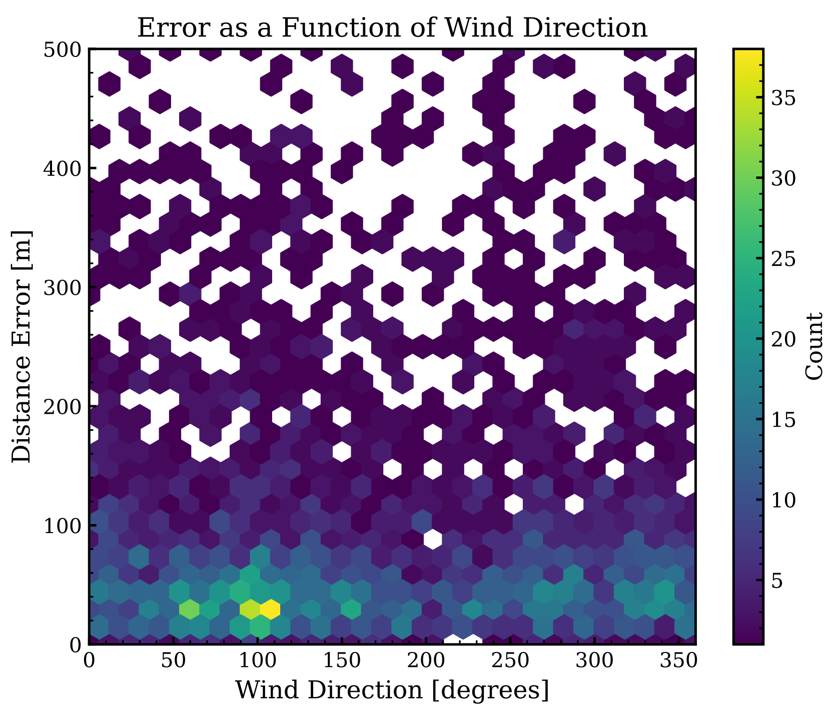

Figure 8: Distance error (m) as a function of wind direction (degrees) on the test set. No clear relationship between wind direction and model performance.

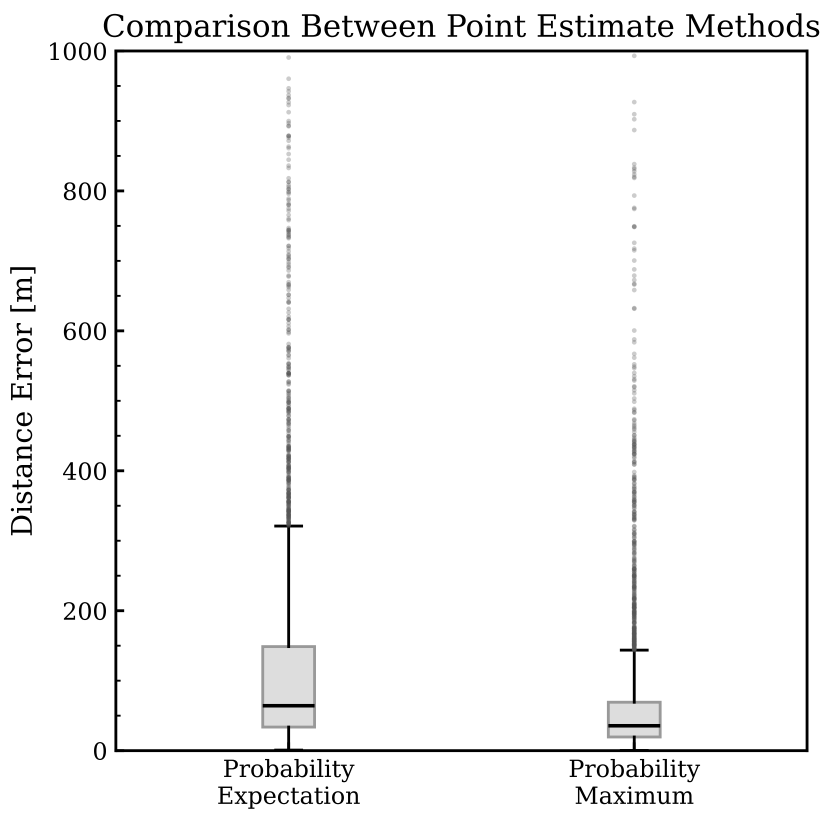

Figure 9: Distance error (m) to expert origin, comparison between expectation and maximum probability method for single origin point prediction (test set). The comparison shows that the median distance error is larger for the probability expectation method than the probability maximum method.